Integrative Biology

Accepted Manuscript

ROYAL SOCIETY OF CHEMISTRY

www.rsc.org/ibiology

Insight

We used three-dimensional cell culture methods to measure the spatial arrangement of cellular metabolism in tumor tissue. A mathematical model was created to interpret microscopic images of cell viability and metabolite concentration profiles. With these tools we showed that, counter to conventional understanding, death can be caused by depletion of glucose, even when oxygen is present. We also showed that apoptosis was the primary mechanism of cell death, and acidity was not caused by lactic acid. Computational analysis showed that the transporter enzymes of glucose and lactate were not saturated, and oxygen uptake was limited by intracellular metabolism. Together these results demonstrate the importance of targeting the metabolic enzymes that control nutrient uptake.

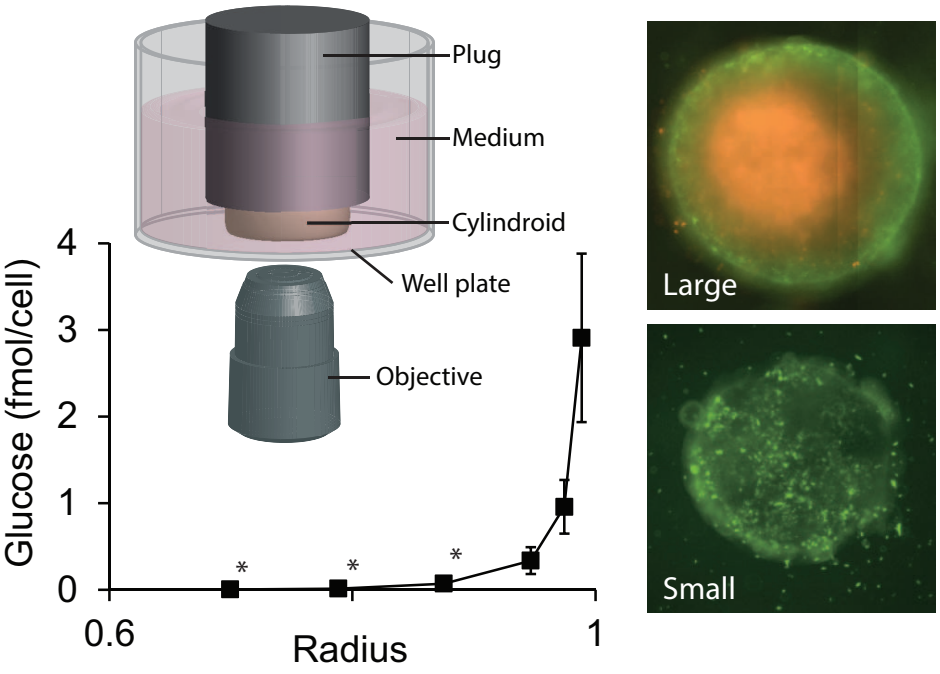

Rapid uptake of glucose and lactate, and not hypoxia, induces apoptosis in three-dimensional tumor tissue culture

Rachel W. Kasinskas, Raja Venkatasubramanian, and Neil S. Forbes

Department of Chemical Engineering
University of Massachusetts, Amherst
Amherst, Massachusetts 01003

Keywords: spheroids, cylindroids, glutamine, lactic acid, glucose, cellular metabolism, diffusion, cellular uptake

Address correspondence to:
Neil S. Forbes
N525 Life Sciences Laboratory
Department of Chemical Engineering
University of Massachusetts, Amherst
686 North Pleasant Street
Amherst, MA 01003
Phone: (413) 577-0132
Fax: (413) 545-1647
Email: forbes@ecs.umass.edu

Abstract

The spatial arrangement of cellular metabolism in tumor tissue critically affects the treatment of cancer. However, little is known about how diffusion and cellular uptake relate to intracellular metabolism and cell death in three-dimensions. To quantify these mechanisms, fluorescent microscopy and multicellular tumor cylindroids were used to measure pH and oxygen profiles, and quantify the distribution of viable, apoptotic and necrotic cells. Spheroid dissociation, enzymatic analysis, and mass spectrometry were used to measure concentration profiles of glucose, lactate and glutamine. A mathematical model was used to integrate these measurements and calculate metabolic rate parameters. It was found that large cylindroids, >500μm in diameter, contained apoptotic and necrotic cells, whereas small cylindroids contained apoptotic but not necrotic cells. The center of cylindroids was found to be acidic but not hypoxic. From the edge to the center, concentrations of glucose, lactate and glutamine decreased rapidly. Throughout the cell masses lactate was consumed and not produced. These measurements indicate that apoptosis was the primary mechanism of cell death; acidity was not caused by lactic acid; and cell death was caused by depletion of carbon sources and not hypoxia. The mathematical model showed that the transporter enzymes for glucose and lactate were not saturated; oxygen uptake was limited by intracellular metabolism; and oxygen uptake was not limited by membrane-transport or diffusion. Unsaturated transmembrane uptake may be the cause of both proliferative and apoptotic regimes in cancer. These results suggest that transporter enzymes are excellent targets for treating well oxygenated tumors.

Introduction

Cellular metabolism and the tumor microenvironment play critical roles in the treatment of cancer[1]. Accelerated metabolism has long been known to be associated with a proliferative phenotype[2] and reduce responsiveness to therapy[3]. Recently there has been renewed interest in targeting metabolic enzymes of cellular metabolism[4] for cancer-specific therapy[5]. However, little is known about how extracellular transport and uptake relates to intracellular metabolism, and how nutrient gradients lead to cell death. Understanding these mechanisms would enable prediction of patient responsiveness to treatment[6]. Development of effective treatments for solid tumors requires quantification of the interactions between metabolism, diffusion and viability.

To investigate how transport affects metabolism it is necessary to use three-dimensional tissue. Measurements in monolayers of cells do not contain spatial gradients and dynamic measurements in animal models are challenging[7]. Several *in vitro* devices have been developed to reproduce the gradients in tumors, including multicellular spheroids[8], cylindroids, and microfluidic devices[9]. These devices mimic the arrangement of cells around blood vessels that control the supply of nutrients[10]. Spheroids are spherical masses of cells surrounded by growth medium (Figure 1A)[11]. Nutrients and oxygen diffuse into the cell mass through the outer edge and are consumed by cells[12]. Most spheroids contain necrotic cores, similar to necrotic regions typical of tumors[13]. Cylindroids are similar to spheroids, but are bounded on the top and bottom by transparent surfaces to enable optical access to the center (Figure 1B)[14]. This accessibility allows for real-time quantification of cellular microenvironment without sectioning or staining[15]. The geometry of cylindroids (Figure 1B) enables quantitative measurement, because light from the central, transport-limited region does not have to pass through successive layers of cells.

The absence of oxygen, or hypoxia, is usually described as the primary cause of cell death in tumors[16]. Using a mathematical model of cancer cell metabolism, we previously predicted that the absence of a carbon nutrients would similarly induce death[17]. Supporting this prediction, we have shown that the primary oxygen-responsive transcription factor, HIF-1α, does not affect metabolism in the absence of glucose[18]. In spheroids, the presence of central hypoxia depends on cell type[19]. Spheroids have been formed that have both hypoxic[20] and well-oxygenated[21] cores. Supplying oxygen directly to the center of cylindroids prevents cell death[22], but the role of carbon nutrients is unknown. Multiple studies have investigated oxygenation of spheroids using oxygen-sensitive dyes[23] and microbeads[24]. To date, only computational methods have been used to investigate the connection between oxygen and carbon transport in tumors[25].

A prominent aspect of cancer cell metabolism is rapid consumption of glucose[2b, 26]. This trait has been recognized for a long time, and is characteristic of rapidly proliferating cells[2a, 27]. The metabolism of glucose and oxygen consumption are closely connected. One link between them is the metabolism of lactate. In the absence of oxygen, glucose is consumed and converted into lactate[28]. However, if substantial oxygen is present, both glucose and lactate can be consumed and converted into carbon dioxide by the TCA cycle[29]. Rapid uptake of glucose and lactate is enabled by high-capacity[30] transporter enzymes: GLUT-family enzymes[31] for glucose and MCT1 for lactate[32]. Recently, it has been shown that MCT1 is necessary for tumor growth[33] and its silencing kills tumor cells in mice[34]. Other metabolic characteristics of tumors are low pH[35], subpopulations of apoptotic cells[36], and rapid consumption of glutamine[37]. Acidic conditions reduce cell proliferation, increase autophagy[38], and increase invasiveness[39]. Glutamine

consumption is essential for proliferating cells that utilize it as either a secondary source of energy or for the production of biosynthetic precursors[40].

To understand the interaction between metabolism and transport, we quantified metabolite concentrations in three-dimensional tumor models. We hypothesized that *depletion of carbon sources, in the absence of hypoxia, causes apoptosis and death,* and *uptake of oxygen is controlled by intracellular metabolism.* To test these hypotheses we used two in vitro models: tumor spheroids and tumor cylindroids, which were developed in our laboratory. Fluorescence microscopy and cylindroids were used to measure pH, oxygen, and the spatial organization of viable, apoptotic and non-viable cells. Spheroid dissociation and GCMS analysis were used to measure intracellular concentrations of glucose, lactate, glutamine and other amino acids as a function of distance from the exterior edge. A mathematical model was used to calculate metabolite uptake rates and determine the dominant mechanisms of transport and uptake. The coupled use of cylindroids, spheroids and computational techniques enabled 1) parallel, spatial measurement of viability, apoptosis, oxygen, and metabolite profiles; and 2) integration of these measurements into a single model of transport and metabolism. These measurements of nutrient diffusion and uptake show how cellular properties create heterogeneity in tumors.

Materials and Methods

Formation of tumor spheroids and cylindroids

All experiments were conducted with LS174T colon carcinoma cells, grown in Dulbecco's Modified Eagle medium with 10% fetal bovine serum at 37^{o}C and 5% CO_2. Spheroids were formed by growing cell aggregates in tissue culture flasks coated with 20mg/ml methacrylate for

14 days (Figure1A). Tumor cylindroids were formed by inserting spheroids into a 96-well plate with a specially designed top plate that was attached to a set of polycarbonate cylindrical plugs (Figure 1B)[14]. The distance between the bottom surface of the well and the bottom of each plug was adjusted to 150±5μm. The diameter of each cylindroid was dependent on the size of the inserted spheroid. Large spheroids form from smaller spheroids with time. Spheroid size is an indication of age. Spheroids ranging in size from 150-1000μm in diameter were selected based on their size, symmetry, and overall integrity. Cylindroids were immersed in 100μL of media, which was added to each well through holes adjacent to each plug in the polycarbonate lid. After being constrained, cylindroids were allowed to equilibrate for 22 hours to establish oxygen and metabolic gradients. Constraining spheroids did not affect cylindroid physiology; solid-stress would dissipate in less than one minute[41].

Measurement of cell viability

Cell viability was measured in small and large cylindroids to determine the effects of cylindroid size and molecular transport on cellular survival. Five small cylindroids, with diameters less than 500μm, and five large cylindroids, with diameters greater than 500μm, were formed and stained with the Live/Dead cytotoxicity kit *(Life Technologies*, Grand Island, NY). After equilibration, the medium in each cylindroid-containing well was replaced with 100μL of DMEM containing 1:250 (v/v) 3,3'-dioctadecylcyloxacarbocyanine($DiOC_{18}(3)$) to stain for viable cells. Cylindroids were incubated in staining solution overnight at 37°C and 5% CO_2. The staining media was removed and cylindroids were washed with 100μL of PBS. These cylindroids were then stained for non-viable cells, by adding 100μL of PBS containing 1:500 (v/v) propidium iodide each well.

The cylindroids were incubated for 3 hours to allow for complete diffusion of the propidium iodide to the center.

To quantify viability as a function of position, fluorescence images were acquired and converted into radial intensity profiles. Images were acquired using an inverted microscope (*Olympus*, Center Valley, PA) equipped with a 10X Plan-APO fluorescence objective (NA=0.40), a 100W HG lamp (*Olympus*), and IPLab software (*Scanalytics*, Fairfax, VA). Two filter sets (*Chroma*, Rockingham,VT) were used: a 470/40 nm band-pass excitation filter, a 495 nm dichroic mirror; and a 525/50 nm band-pass emission filter (to image viable cells) and a 535/50 nm band-pass excitation filter; a 565 nm dichroic mirror; and a 590 nm long-pass emission filter (to image dead cells). Tiling macros were used to acquire images of cylindroids larger than 400μm in diameter. Four panels (size: 665.8 x 873.9 μm), acquired with a 10X objective, were joined together to create an image that could be centered on larger cylindroids. Tiled images allowed for more accurate quantification of fluorescence intensity. Radial profiles were generated from fluorescent images by first measuring the radius of each cylindroid using transmitted light images. The fluorescence intensity of pixels, within circular annuli from cylindroid centers ($r=0$) to edges ($r=R$), were averaged using a script in ImageJ (NIH Research Services Branch). Profiles were corrected for auto-fluorescence by subtracting fluorescence intensities of images acquired prior to the addition of fluorescent dyes. Fluorescence values were normalized by the maximum intensity in each profile.

Measurement of apoptosis

The extent of apoptosis was measured in small and large cylindroids using the CaspGLOW Red Caspase-3 staining kit (*BioVision, Inc.*, Mountain View, CA). This assay utilizes the caspase-3 inhibitor, DEVD-FMK conjugated to sulfo-rhodamine (Red-DEVD-FMK), as an *in situ* fluorescent marker. DEVD-FMK irreversibly binds to activated caspase-3 in apoptotic cells. After cylindroids were formation and allowed to equilibrate, 100μL of 1:1000 (v/v) Red-DEVD-FMK in DMEM was added to each well. Cylindroids were incubated in staining solution at 37°C and 5% CO_2 for 2 hours. Fluorescence images were acquired and converted into radial profiles, corrected for auto-fluorescence, and normalized as described above. A 535/50 nm excitation, 565 nm dichroic, and 590 emission filter set (*Chroma*) was used.

Measurement of oxygen profiles

Oxygen profiles were measured in tumor cylindroids using ruthenium-tris(4,7-diphenyl-1,10-phenanthroline)dichloride (Ru-dpp; *Sigma-Aldrich*, St. Louis, MO). The Ru-dpp dye is intensely fluorescent at low oxygen concentrations and less fluorescent at ambient concentrations. The Ru-dpp assay was calibrated by acquiring fluorescence images of empty wells filled with 100μL of 1:1000 (v/v) Ru-dpp in DMEM and measuring the average fluorescence intensity. Intensities were measured for wells exposed to ambient air (159 mmHg O_2; $I_{ambient}$) and exposed to pure nitrogen (0 mmHg O_2; I_{N_2}). Background intensities for the calibration ($I_{calibration}^{background}$) were measured for wells filled with DMEM and no Ru-dpp. To measure oxygen profiles, cylindroids were formed and equilibrated as described above. Images of these cylindroids were acquired to determine background intensities ($I_{measured}^{background}$) and to correct for auto-fluorescence. A 100μL solution of 1:1000 (v/v) Ru-dpp in DMEM was added to each cylindroid-containing well.

Cylindroids were incubated in staining solution overnight at 37°C and 5% CO_2. Fluorescence images were acquired and converted into radial profiles as described above. Local oxygen concentrations were determined from the cylindroid radial intensity profiles based on a straight-line calibration: $P_{O_2} = P_{O_2}^{ambient}\left[\left(I_{measured} - I_{measured}^{background}\right) - \left(I_{N_2} - I_{calibration}^{background}\right)\right] \Big/ \left(I_{ambient} - I_{N_2}\right)$.

Measurement of pH profiles

Profiles of extracellular pH were quantified in tumor cylindroids using 2',7'-bis-(2-carboxyethyl)-5-(and-6)-carboxyfluorescein, (BCECF; *Invitrogen*, Carlsbad, CA). The fluorescence of BCECF is sensitive to pH at 495nm and not at 440nm, enabling pH measurement independent of dye concentration. Images were acquired with a specific BCECF filter set (*Chroma*) with two excitation filters (440/20 and 495/10nm), a dichroic mirror (515nm) and an emission filters (535/25nm). Fluorescent calibration measurements were taken in medium at pH 3.78, 7.55, and 11.2 to determine the linear relationship between pH and fluorescence, $pH = 1.21 \cdot R + 5.15$, where the fluorescence ratio, R, is I_{440}/I_{495}. To determine the pH in cylindroids, 54 cylindroids were formed as described above. After equilibration, 100 µL of 1:1000 (*v/v*) BCECF in DMEM was added to each cylindroid-containing well. Cylindroids were incubated in staining solution for 17 hours at 37°C and 5% CO_2. Fluorescence images at the two emission wavelengths, 495 and 440nm, were acquired and converted into radial profiles. Profiles were corrected for auto-fluorescence by subtracting intensities of background images, acquired prior to the addition of the fluorescent BCECF dye. Fluorescence intensities at each radial position were converted into pH values using the calibrated relationship. Radial positions were normalized and the profiles were averaged across all cylindroids.

Measurement of intracellular metabolites in tumor spheroids

Radial concentration profiles of intercellular metabolites were determine by dissociating spheroids into individual cell layers[42]. The dissociation procedure was repeated twice, once for enzymatic analysis and once for measurement of amino acids by GCMS. Spheroids were formed by inoculating a single-cell suspension of LS174T cells at a concentration of 1000cells/ml into T-flasks coated with methacrylate. Spheroids were grown in flasks for 14 days, transferred to a 100 mL stirred vessel, and grown for an addition five days to ensure uniformity. Spheroids, 400 - 600 μm in diameter, were removed from the stirred vessel, separated into three equal groups and media was removed. Spheroids were washed twice with PBS to remove residual media, which would neutralize the trypsin solution.

Each group of spheroids was transferred to a racetrack device, which consisted of two concentric petri dishes, one glued inside the other. The inclusion of a smaller petri dish inside the larger dish ensured that spheres did not clump at the center during oscillation[42]. PBS was removed and replaced with 5ml of 0.5% trypsin in PBS. The racetrack was rotated at 80 RPM and 37°C. After 20 minutes, dissociated cells in the PBS/trypsin were removed without removing the spheroids, and 10ml DMEM was added to stop the trypsin reaction. The spheroids in the racetrack were rinsed with PBS and another 5ml of 0.5% trypsin was added to remove the next cell layer. Dissociated cells were centrifuged for 5 minutes, resuspended in 10ml PBS, and counted by hemocytometer. Each layer of dissociated cells was then centrifuged for an addition 5 minutes and resuspended in 10ml water. Samples were homogenized to break cell membranes and release cellular contents. Homogenized samples were submerged in liquid nitrogen and lyophilized

overnight. The dissociation procedure was repeated to remove five layers of cells. The distance from the spheroid outer edge to each dissociated layer was calculated using

$$d = \frac{1}{2}\left((dc \cdot (D_t^3 - D_n^3) + D_n^3)^{1/3} - D_n\right) \quad (1)$$

where D_t is the spheroid diameter, D_n is the necrotic center diameter, and dc is the cumulative fraction of cells removed[42].

The concentrations of intracellular metabolites were determined by enzymatic analysis and GCMS. For enzymatic analysis, lyophilized samples was reconstituted with 100µl water and the concentration of glucose, lactate, glutamate, and glutamine were directly measured using a biological analyzer (*YSI*, Yellow Springs, OH). For GCMS analysis, lyophilized samples were derivatized in 100µL ofdimethylformamide (DMF) and 100 µL of N-methyl-N-(tert-butyldimethyl-silyl) trifluoroacetamide (MTBSTFA) containing 1% tert-dutyldimethylchlorosilane (TBDMCS). The TBDMCS was added as a catalyst to produce tert-butyldimethyl silyl (TBDMS) amino-acid derivatives[43]. Each sample was incubated at 70°C for 1 hour before injection into the GCMS (*Agilent*, Santa Clara CA), which was equipped with a 30m x 0.25mm DB-5 capillary column (0.25 µm film thickness, *Supelco*, Bellefonte, PA) and a time-of-flight mass spectrometer (*Micromass*, Beverly, MA). The injector temperature was 300°C, the detector temperature was 280°C, and the injection volume was 10µL. The relative molar concentration of each amino acid in each sample was calculated from standard curves with standards of known concentrations.

Data assessment and statistical analysis

Two different culture techniques (spheroids and cylindroids) were used in this study. For viability, death, and apoptosis measurements, cylindroids of different size (small and large) were compared. The effect of location was determined by comparing the binned average of different radial regions (peripheral and central) across cylindroid populations. Radial comparisons were made with fluorescence measurements of oxygen and pH, using separate cylindroid populations for each. Metabolite concentrations were determined in three groups of spheroids for enzymatic analysis and three groups for GCMS. Each annular region was a separate population of cells removed from the exterior of spheroids by dissociation. Data are reported as means ± standard errors. Hypothesis testing was conducted using Student's t-test with two-tailed analysis. Statistical significance was assigned at $P<0.05$.

Mathematical model of transport and metabolism

A mathematical model was used to interpret the radial concentration profiles of glucose, oxygen, and lactate. Parameters were determined numerically by fitting the model to experimentally measured radial concentration profiles of glucose, lactate, and oxygen. The model was solved using finite differences and constrained nonlinear optimization in Matlab (*Mathworks*, Natick, MA). Intracellular concentrations of glucose and lactate, with units of fmol/cell, were converted into bulk units, μmol/L, based on an average cell size of 1.64 pL/cell. Oxygen partial pressures (in mmHg) were converted to concentration units (μmol/L) using Henry's law. Diffusion coefficients for glucose, lactate and oxygen were determined from previous measurements in spheroids[23, 40]. Optimization was used to determine six parameters: Q_{gluc}^{max}, Q_{Lac}^{max}, Q_{Ox}^{max}, Km_{gluc},

Km_{Lac}, and Km_{Ox}. For nutrients with unsaturated uptake ($Km_i \gg C_i$), parameters were replaced with first-order rate constants $k_i = Q_i^{max}/Km_i$.

Results

Cell viability in tumor cylindroids

The location of viable and dead tissue was identified in cylindroids was using fluorescence microscopy (Fig. 2). Fluorescent dyes were used to specifically identify proliferating (Fig. 2A; center), apoptotic (Fig. 2B; right), and necrotic (Fig. 2A; right) cells. Small cylindroids, with diameters less than 500μm, contained only viable cells and no dead cells (Fig. 2A). In comparison, large cylindroids, with diameters greater than 500μm, contained distinct regions of viable and necrotic cells (Fig. 2A). Both small and large cylindroids contained apoptotic cells (Fig. 2B). The co-localization of the two stains in large cylindroids indicates that cells had permeable membranes and died after activation of caspase-3.

Fluorescence values were averaged as a function of normalized radial distance to create viability profiles for populations of small (Fig. 2C; *n*=5 for live/dead; *n*=6 for apoptosis) and large (Fig. 2D; *n*=5 for live/dead, *n*=3 for apoptosis) cylindroids. Viability profiles were consistent for all small and large cylindroids; the average relative error for these measurements was less than 7%. For small cylindroids, viable cells were located across the entire diameter and no dead cells were observed (Fig. 2C). The extent of apoptosis increased from the outer edge toward the center. In large cylindroids, cell viability was greatest at the outer edge and decreased toward the center (Fig. 2D). The extent of necrosis was low at the periphery and increased toward the center. Similar to small cylindroids, the extent of apoptosis increased from the outer edge toward the

center. The apparent drop in viability in the outermost annulus of both profiles (Fig. 2C&D) is an artifact caused by cylindroid geometry. Cylindroids do not have a straight vertical edge, but bulge slightly above the focal plane (Fig. 1B).

Cell populations in small and large cylindroids were compared by averaging fluorescence intensities in the central and peripheral regions, defined as the inner and outer 10% of the total radius (Fig. 2E). In large cylindroids, cell viability was greater at the periphery than the center ($P<0.001$) and cell death was greater in the center compared to the periphery ($P<0.001$; Fig. 2E). In small cylindroids, there was no difference in viability or death with position (Fig. 2E). For both small and large cylindroids, there was more apoptosis at the center than the periphery ($P<0.001$; Fig. 2E). In the center, viability was greater in small cylindroids ($P<0.001$), and death was greater in large cylindroids ($P<0.001$; Fig. 2E).

Oxygen and pH gradients in tumor cylindroids

The extracellular concentration of oxygen was measured in cylindroids (Fig. 3A) using a ruthenium dye (Ru-dpp) that is florescent in low oxygen environments and is quenched in the presence of oxygen (Fig. 3B). After administration, fluorescence from ruthenium quickly equilibrated indicating complete coverage of the dye across the width of cylindroids. In a typical cylindroid, the lowest brightest fluorescence was observed in a ring between the edge and center (Fig. 3A). Fluorescent images of cylindroids (n=14) were converted into radial oxygen profiles (Fig. 3C) based on calibrations of ruthenium in low and high oxygen environments. In the average oxygen profile (Fig. 3C), there was a decreasing gradient from the cylindroid edge to a minimum at r/R=0.8 and a slight increase toward the center. The extracellular oxygen

concentration in the entire interior region ($r/R \leq 0.975$) was lower than at the edge ($P<0.01$, Fig. 3C). For the whole cylindroid population, the minimal oxygen concentration occurred at an average distance of 82±4μm from the edge. Based on a definition of hypoxia as less than 10mmHg[44], no region of the cylindroids, including the centers (P_{O2}=20.6mmHg), were hypoxic (Fig. 3C). These relationships were conserved for cylindroid of all sizes (R=280 to 479μm).

Extracellular pH in cylindroids was measured with BCECF, a fluorescent dye that is sensitive to pH at 495nm (Fig. 3D). Radial pH profiles (Fig. 3E) were generated from fluorescence images (Fig. 3D) from a population of cylindroids (n=54). The centers of cylindroids ($r/R<0.5$) were slightly acidic (pH=6.92; $P<0.005$) and the profiles had a maximum value of 7.03 at r/R=0.875 (Fig. 3E). Extracellular pH formed a plateau beginning at r/R = 0.5 that was constant through the cylindroid centers. The pH in this central region ($r/R \leq 0.5$) was significantly lower than at the maximum ($P<0.005$, Fig. 3E). Within the cylindroid population, the maxima and plateaus were located at average distances of 36±10 and 125±11μm from the edge. There was no observed relationship between cylindroid diameter and central pH value. The decrease towards acidic pH values at cylindroid centers was observed for all cylindroids.

Metabolite concentration profiles

Metabolites concentrations were measured by dissociating successive layers of cells from spheroids (Fig. 4&5). Two different analytical techniques were used to measure concentration: enzymatic analysis (Fig. 4) and GCMS (Fig. 5). Concentrations of glucose, lactate, and glutamine (Fig. 4A-C) were lower in central layers compared to the outer layer ($p<0.05$; n=3). The profiles of these three metabolites decreased exponentially from the edge to the center (Fig.

4A-C). The concentrations were less than 20% of the value at the outer edge by the third layer for all three. This layer was located at normalized radius of 0.95, which was equivalent to 15μm from the edge. The concentration of these nutrients was vanishingly small in the central region (Fig. 4A-C). In the two innermost layers, with normalize radii of 0.70 and 0.79, the average concentrations of glucose and glutamine were less than 1% of the values at the edge. The concentration profile for glutamate had a different pattern; it did not decrease toward the center and was relatively constant with radius (Fig. 4D).

The concentration profile of intracellular amino acids decreased toward the center of cylindroids, similar to glucose (Fig. 5). The concentration of all measured amino acids was lower in the inner layer, at r/R=0.70, than at the outer edge ($P<0.05$; n=3). The decrease in the concentration of essential amino acids (Fig. 5A) was steeper than for non-essential amino acids (Fig. 5B). In the inner layer, the average concentrations of valine, leucine, and isoleucine (Fig. 5A) were 5% of the outer layer. The average concentrations of alanine, gylcine, proline, serine, and aspartate (Fig. 5B) in the inner layer were comparatively higher, and was 20% of the value in the outer layer.

Mathematical modelling of cellular metabolism

A mathematical model was used to interpret the metabolite profiles of glucose, lactate and oxygen (Fig. 6). The model coupled molecular diffusion and intracellular metabolism, and was based on a model previously developed in our laboratory[45]. Nutrient transport was modeled by balancing diffusion with cellular uptake

$$D_i \nabla^2 C_i = Q_i \qquad \left.\frac{\partial C_i}{\partial r} = 0\right|_{r=0} \qquad C_i = C_{i,bulk}\big|_{r=R} \qquad (2)$$

where, C_i is the local nutrient concentration, Q_i is the nutrient uptake rate, and i represents glucose, oxygen, or lactate. The diffusion coefficients, D_i, for glucose, lactate, and oxygen were experimentally measured previously[23, 40]: 1.05×10^{-6}, 1.78×10^{-6}, and 1.82×10^{-5}, respectively. The average radius was 245 μm. The uptake rate expressions, Q_i, balance the kinetics of metabolite uptake (Eq. 3) with the stoichiometry of intracellular metabolism (Eq. 4).

$$Q_{Gluc} = \frac{Q_{Gluc}^{max} C_{Gluc}}{Km_{Gluc} + C_{Gluc}} \qquad Q_{Ox}^{trans} = \frac{Q_{Ox}^{max} C_{Ox}}{Km_{Ox} + C_{Ox}} \qquad Q_{Lac}^{trans} = \frac{Q_{Lac}^{max} C_{Lac}}{Km_{Lac} + C_{Lac}} \tag{3}$$

$$\begin{aligned} Q_{Ox} &= \min\left(Q_{Ox}^{trans}, 6Q_{Gluc} + 3Q_{Lac}^{trans}\right) \\ Q_{Lac} &= -2Q_{Gluc} + Q_{Ox}/3 \end{aligned} \tag{4}$$

The transmembrane uptake rates, Q_i^{trans}, represent the maximum uptake rates based on metabolite availability in the extracellular environment and are described using Michaelis–Menten kinetics (Eq. 3). The parameters, Q_i^{max} and Km_i are the maximum uptake rates and saturation concentrations of metabolite i. Balanced uptake rates (Q_{Gluc}, Q_{Ox} and Q_{lac}) are limited by the stoichiometry of intracellular metabolism (Eq. 4). These two expressions account for the primary metabolic reactions of glycolysis and the TCA cycle[45]. They are based on three assumptions: 1) cells consume glucose when it is available, 2) oxygen uptake is limited by either transport or the availability of carbon sources, and 3) lactate can be consumed as a carbon source when the concentration of glucose is low and the concentration of oxygen is high. In this model glucose and oxygen can only be consumed and lactate can be produced or consumed[45]. Explicit terms for cell viability were not included because all observed metabolic changes (Fig. 4) occurred within viable tissue (Fig. 2).

The uptake rates of glucose and lactate were obtained by fitting the model (Eq. 2-4; Fig. 6A-C) to the measured radial concentration profiles (Fig. 4). Over the entire radius, the uptake rates of glucose and lactate were linearly dependent on concentration (P<0.001) and did not saturate, indicating that uptake kinetics were first order ($Km_i \gg C_i$ and $Q_i^{trans} = k_i C_i$ where $k_i = Q_i^{max}/Km_i$). The first-order rate constants, k_{gluc} and k_{lac} were calculated to be 13.82 and 20.60 sec^{-1}, respectively. At all positions, lactate was consumed (Fig. 6B) and the uptake of oxygen was stoichiometrically controlled (Fig. 6C). Because oxygen uptake was not dependent on transmembrane transport, values for Q_{Ox}^{max} and Km_{Ox} were not determined. Oxygen uptake (Q_{Ox}) was equal to the stoichiometric limit of intracellular metabolism (Eq.4; $6Q_{Gluc} + 3Q_{Lac}$) across the entire radius (Fig. 6D).

To demonstrate the effect of a hypothetical limit on transmembrane oxygen uptake, model parameters were artificially modified (Fig. 6E). If the maximum rate of oxygen transport (Q_{Ox}^{max}) was reduced, uptake rates would have been lower (compare Fig. 6E to 6D). Limited oxygen uptake would have altered observed metabolic profiles. At the outer edge of the cell mass, lactate would have been produced, not consumed (Fig. 6E). This effect would have been detected as an increase in lactate concentration at the edge, rather than the observed exponential decrease (Fig. 6B).

The availability of oxygen throughout the tumor mass (Fig. 6C) decoupled lactate transport (Eq. 2,3) from intracellular stoichiometry (Eq. 4). Because C_{Ox} was large, Q_{Ox}^{trans} was greater than the limit of intracellular stoichiometry. As the lower value in the minimization expression (Eq. 4), oxygen uptake was given by $6Q_{gluc} + 3Q_{lac}^{trans}$. In this regime, $Q_{lac} = -2Q_{gluc} + \left(6Q_{gluc} +\right.$

$3Q_{lac}^{trans}\big)/3 = Q_{Lac}^{trans}$. This decoupling enabled the transport of glucose and lactate to be analyzed independently. Thiele moduli ($\sqrt{R^2 k_i / D_i}$) for glucose and lactate were calculated to be 88.9 and 83.3, indicating that uptake was faster than diffusion for whole spheroids. This relation was not true for oxygen, which was not limited by diffusion or transmembrane uptake (Fig. 6E). Although the transport of glucose and lactate was diffusion-limited for whole spheroids, the kinetics of transmembrane transport greatly affected local uptake rates (Fig. 6F). At the measured kinetic rate, the uptake of glucose was high at the outer edge and decreased steeply toward the center (Fig. 6F). Artificially reducing the glucose rate constant (k_{gluc}) 4 and 10 fold, reduced uptake at the edge and increased uptake towards the center (Fig. 6F).

Discussion

The measurement of viability and nutrient concentrations in three-dimensional masses of tumors cells identified several important characteristics of cell metabolism that depend on position relative to the nutrient source. Apoptosis was present in both small and large cylindroids, but necrosis was only seen in large cylindroids (Fig. 2). The center of the cylindroids was not hypoxic (Fig. 3), but there were steep gradients of glucose, glutamine, and lactate (Fig. 4). The rapid decrease in glutamine concentration (Fig. 4C) indicated a high rate of glutamine uptake. Measured concentration profiles (Fig. 4) were fit to a mathematical model (Fig. 6), and showed that lactate was rapidly consumed and not produced (Fig. 6B), as is often thought to occur in tumors[46]. The centers of cylindroids was observed to be acidic (Fig. 3) and most amino acids were consumed (Fig. 5). Most of these metabolic patterns are representative of all tumors, including rapid uptake of glucose and glutamine. Although the absence of hypoxia cannot be

generalized to all tumors, rapid lactate consumption would be a characteristic of well-oxygenated tumors.

Apoptosis was primary mechanism of cell death

In these cell masses composed of colon carcinoma cells, apoptosis was the primary cause of cell death (Fig. 2). The presence of apoptosis in the center of small cylindroids (Fig. 2B), and the absence of necrosis (Fig. 2A) suggests that apoptosis occurred prior to necrosis. The centers of large cylindroids, on the other hand, were both apoptotic (Fig. 2B) and necrotic (Fig. 2A). Comparison of small and large cylindroids indicates how cell masses change with time. Large spheroids form from smaller spheroids that have grown. The patterns of apoptosis and necrosis in larger spheroids appeared because of continued metabolism and growth of small spheroids. As spheroids grew larger than 500 μm in diameter, the inner 77% of the volume had almost no available carbon source (Fig. 4). The dependence on size suggests that nutrient deprivation first induced apoptosis, which was followed by necrotic death.

Cell death was caused by depletion of carbon sources and not hypoxia

In the observed cell masses, hypoxia was not observed (Fig. 3) and was not the cause of death. The primary reason for the absence of hypoxia, based on the mathematical model (Fig. 6), was rapid consumption of glucose, which killed cells close to the edge and enabled oxygen to diffuse to the dead inner core. While hypoxia is often of the cause of cell death in tumors *in vivo*[16b], these measurements of viability show that cell death (Fig. 2) can occur in the presence of sufficient oxygen (Fig. 3). In these cultures, nutrient depletion (Fig. 4&5) was the primary cause

of death. The rapid decrease in lactate concentration toward the center of cylindroids (Fig. 4B) indicates the extent that the carbon supply was limiting. Glutamine depletion (Fig. 4C) was also an important factor contributing to cell death. We have previously shown in cylindroids that glutamine depletion induces apoptosis[15]. For these cells, death was not caused by buildup of lactate (Fig. 4B) or depletion of non-essential amino acids, which were not completely exhausted (Fig. 5B).

These results support predictions generated by a mathematical model previously developed in our laboratory[47]. This model predicted that, although hypoxia is often the primary cause of cell death, cell physiology and nutrient availability can alter this dependence, and carbon depletion can be the primary cause of death. The implication of this observation is that hypoxia is not necessary for cell death *in vivo*. Cells will die because of lack of nutrients even if they have sufficient oxygen.

Carbon consumption for biosynthesis

The consumption of amino acids (Figs. 6&7) was most likely for biosynthesis of proteins and macromolecules. Four different patterns of consumption were observed suggesting four different metabolic roles: 1) glutamine was rapidly consumed (Fig. 4C); 2) essential amino acids were completely consumed (Fig. 5A); 3) non-essential amino acids were consumed, but not completely (Fig. 5B); and 4) glutamate was not consumed (Fig. 4D). For comparison, the average change in concentration over the outer 5% of the radius for glutamine, essential, and non-essential amino acids was 2.1, 0.20, and 0.020 fmol·cell^{-1}, respectively (Figs. 4&5). The difference between essential and non-essential amino acids suggests that non-essential amino

acids are consumed for biosynthetic routes other than protein synthesis[40b]. Cells consume glutamine for two purposes: to synthesize nucleotides, fatty acids and other amino acids or to generate energy[2b]. The consumption of glutamine in the presence of available glucose (Fig. 4) suggests that glutamine was primarily utilized for biosynthesis. This explanation is supported by isotopic labeling experiments that showed that cancer cells predominantly use glutamine for biosynthesis[18, 48]. Glutamate was not consumed (Fig. 4D) because it is a side-produce of rapid glutamine consumption, and its intracellular concentration is usually high, reducing the driving force for uptake[40b].

Acidity not caused by lactic acid

The measurement of low pH (Fig. 3) and low intracellular lactic acid (Fig. 4B) indicates that lactic acid was not the source of acidity. It was most likely caused by the production of carbonic acid, as we have shown previously in mice[46]. In glycolysis-impaired tumors, lactic acid production is negligible and significant acidification is still observed[49]. Comparatively, in monolayer cultures, a high glycolytic flux, is usually coupled with high rates of lactate production[48]. This distinction illustrates the importance of three-dimensional cultures for quantifying cellular metabolism. In spheroids, glucose and lactate were consumed in parallel (Fig. 4), a phenomenon not seen monolayers[48].

Kinetics of glucose and lactate uptake

The mathematical model of central metabolism (Eq. 2-4; Fig. 6) enable interpretation of the measured concentration profiles. The most significant observations were that 1) oxygen uptake was limited by the stoichiometry of primary metabolism, 2) oxygen uptake was not limited by

membrane-transport or mass transfer through the cell mass, and 3) the saturation constants (K_m) of glucose and lactate uptake were high, and uptake was first-order. The model showed that the high rate of lactate uptake was enabled by an abundant supply of oxygen (Fig. 6). Oxygen was necessary for catabolism of lactate, which can only provide cellular energy via the TCA cycle[2b]. Limited oxygen would have resulted in lactate production (Fig. 6E), not consumption as was observed (Fig. 4B).

The first-order kinetic rates of lactate and glucose indicates that the transporter enzymes for glucose and lactate (e.g. GLUT and MCT1) were not near saturation. These high saturation concentrations would explain the high glycolytic rates seen in cancer. Unrestricted uptake could also be the cause of cell viability patterns seen in tumors. In well-supplied tissue, rapid uptake of carbon would enable rapid cell growth. However, it would also rapidly deplete the local environment. This depletion would create cellular regions that are starved for nutrients, even when oxygen was available (Fig. 6F). This in turn would lead to apoptosis and cell death (Fig. 2). The importance of the transporter enzymes was demonstrated by computationally reducing the uptake rate constants (Fig. 6F), which decreased consumption at the edge and increased consumption in the center. In turn, this inhibition of transmembrane transport would decrease proliferation in supplied regions and decrease apoptosis far from nutrient sources (Fig. 2). In these observed tumor masses, transporter proteins controlled metabolism because neither oxygen uptake nor availability were limiting (Fig. 6D,E). Biologically, transport capacity is dependent on both catalytic rate and enzyme expression. This suggests that the expression and kinetics of GLUT and MCT1 should be investigated and both of these enzymes should be further explored as drug targets[34] for well-oxygenated tumors.

Conclusions

Measurement of cell viability and metabolite concentrations identified several unexpected characteristics of cancer cells grown in three-dimensional culture. It was found that center of the colon-carcinoma cylindroids were not hypoxic; that lactate was consumed, not produced; that there were steep gradients of glucose and glutamine; and that apoptosis was primary mechanism of cell death. Together these measurements indicated that nutrient gradients, and not hypoxia, caused apoptosis and cell death. Integration of these results into a coupled computational model of transport and metabolism identified several significant metabolic characteristics of cells in three-dimensional tissue. Cellular uptake of glucose and lactate was not saturated and nearly first-order. Oxygen uptake was limited by the stoichiometry of intracellular metabolism, and not by membrane transport or diffusion through the cell mass. These results are important because they suggest that the transporter enzymes of glucose and lactate control the fate of cancer cells in tumors, and are targets for treating oxygenated tumors.

Acknowledgements

We gratefully acknowledge financial support from the National Institutes of Health (Grant Nos. R21CA112335 and R01CA120825), the National Science Foundation (Grant No. 1159689).

References

1. (a) R. Venkatasubramanian, M. A. Henson, N. S. Forbes, Integrating cell-cycle progression, drug penetration and energy metabolism to identify improved cancer therapeutic strategies. *Journal of theoretical biology* 2008, *253*. 98-117, DOI: 10.1016/j.jtbi.2008.02.016; (b) R. Cairns, I. Papandreou, N. Denko, Overcoming physiologic barriers to cancer treatment by molecularly targeting the tumor microenvironment. *Mol Cancer Res* 2006, *4*. 61-70.
2. (a) O. Warburg, Ist die aerobe Glykolyse spezifisch für die Turmoren? *Biochem Zietschrift* 1929, *204*. 482; (b) N. S. Forbes, D. S. Clark, H. W. Blanch, in *Bioreaction Engineering: Modeling and Control*, ed. K. Schügerl, K. H. Bellgardt. Springer Verlag: Berlin, 2000, p Chap 4.4.
3. O. Tredan, C. M. Galmarini, K. Patel, I. F. Tannock, Drug resistance and the solid tumor microenvironment. *J Natl Cancer Inst* 2007, *99*. 1441-54.
4. (a) R. A. Cairns, I. S. Harris, T. W. Mak, Regulation of cancer cell metabolism. *Nature Reviews Cancer* 2011, *11*. 85-95, DOI: 10.1038/nrc2981; (b) H. R. Christofk, M. G. Vander Heiden, M. H. Harris, A. Ramanathan, R. E. Gerszten, R. Wei, M. D. Fleming, S. L. Schreiber, L. C. Cantley, The M2 splice isoform of pyruvate kinase is important for cancer metabolism and tumour growth. *Nature* 2008, *452*. 230-U74, DOI: 10.1038/nature06734; (c) M. J. Ovens, A. J. Davies, M. C. Wilson, C. M. Murray, A. P. Halestrap, AR-C155858 is a potent inhibitor of monocarboxylate transporters MCT1 and MCT2 that binds to an intracellular site involving transmembrane helices 7-10. *Biochem J* 2010, *425*. 523-530, DOI: 10.1042/bj20091515; (d) P. Nicklin, P. Bergman, B. L. Zhang, E. Triantafellow, H. Wang, B. Nyfeler, H. D. Yang, M. Hild, C. Kung, C. Wilson, V. E. Myer, J. P. MacKeigan, J. A. Porter, Y. K. Wang, L. C. Cantley, P. M. Finan, L. O. Murphy, Bidirectional Transport of Amino Acids Regulates mTOR and Autophagy. *Cell* 2009, *136*. 521-534, DOI: 10.1016/j.cell.2008.11.044.
5. (a) D. A. Tennant, R. V. Duran, E. Gottlieb, Targeting metabolic transformation for cancer therapy. *Nature Reviews Cancer* 2010, *10*. 267-277, DOI: 10.1038/nrc2817; (b) J. I. Hanai, N. Doro, P. Seth, V. P. Sukhatme, ATP citrate lyase knockdown impacts cancer stem cells in vitro. *Cell Death Dis.* 2013, *4*. DOI: e696
10.1038/cddis.2013.215; (c) J. B. Ye, A. Mancuso, X. M. Tong, P. S. Ward, J. Fan, J. D. Rabinowitz, C. B. Thompson, Pyruvate kinase M2 promotes de novo serine synthesis to sustain mTORC1 activity and cell proliferation. *Proceedings of the National Academy of Sciences of the United States of America* 2012, *109*. 6904-6909, DOI: 10.1073/pnas.1204176109.
6. R. Venkatasubramanian, R. B. Arenas, M. A. Henson, N. S. Forbes, Mechanistic modelling of dynamic MRI data predicts that tumour heterogeneity decreases therapeutic response. *British journal of cancer* 2010, *103*. 486-97, DOI: 10.1038/sj.bjc.6605773.
7. L. A. Kunz-Schughart, J. P. Freyer, F. Hofstaedter, R. Ebner, The use of 3-D cultures for high-throughput screening: the multicellular spheroid model. *J Biomol Screen* 2004, *9*. 273-85.
8. (a) E. A. Mandujano-Tinoco, J. C. Gallardo-Perez, A. Marin-Hernandez, R. Moreno-Sanchez, S. Rodriguez-Enriquez, Anti-mitochondrial therapy in human breast cancer multi-cellular spheroids. *Biochimica Et Biophysica Acta-Molecular Cell Research* 2013, *1833*. 541-551, DOI: 10.1016/j.bbamcr.2012.11.013; (b) G. Mehta, A. Y. Hsiao, M. Ingram, G. D. Luker, S. Takayama, Opportunities and challenges for use of tumor spheroids as models to test drug delivery and efficacy. *Journal of Controlled Release* 2012, *164*. 192-204, DOI: 10.1016/j.jconrel.2012.04.045.

9. (a) B. J. Toley, D. E. Ganz, C. L. Walsh, N. S. Forbes, Microfluidic Device for Recreating a Tumor Microenvironment. *J Vis Exp* 2011, *DOI: 10.3791/2425*; (b) C. L. Walsh, B. M. Babin, R. W. Kasinskas, J. A. Foster, M. J. McGarry, N. S. Forbes, A multipurpose microfluidic device designed to mimic microenvironment gradients and develop targeted cancer therapeutics. *Lab on a chip* 2009, *9*. 545-54.
10. (a) G. Hamilton, Multicellular spheroids as an in vitro tumor model. *Cancer Lett* 1998, *131*. 29-34; (b) P. Vaupel, F. Kallinowski, P. Okunieff, Blood flow, oxygen and nutrient supply, and metabolic microenvironment of human tumors: a review. *Cancer Res* 1989, *49*. 6449-65.
11. R. M. Sutherland, R. E. Durand, Growth and cellular characteristics of multicell spheroids. *Rec. Res. Camcer Res.* 1984, *95*. 24-49.
12. J. J. Casciari, S. V. Sotirchos, R. M. Sutherland, Glucose diffusivity in multicellular tumor spheroids. *Cancer Research* 1988, *48*. 3905-3909.
13. R. M. Sutherland, Cell and environment interactions in tumor microregions: the multicell spheroid model. *Science* 1988, *240*. 177-84.
14. R. W. Kasinskas, N. S. Forbes, Salmonella typhimurium specifically chemotax and proliferate in heterogeneous tumor tissue in vitro. *Biotechnol Bioeng* 2006, *94*. 710-21.
15. B. J. Kim, N. S. Forbes, Single-cell analysis demonstrates how nutrient deprivation creates apoptotic and quiescent cell populations in tumor cylindroids. *Biotechnol Bioeng* 2008, *101*. 797-810.
16. (a) W. F. Mueller-Klieser, R. M. Sutherland, Oxygen tensions in multicell spheroids of two cell lines. *Br J Cancer* 1982, *45*. 256-64; (b) P. Vaupel, D. K. Kelleher, M. Hockel, Oxygen status of malignant tumors: pathogenesis of hypoxia and significance for tumor therapy. *Semin Oncol* 2001, *28*. 29-35; (c) G. L. Semenza, Regulation of cancer cell metabolism by hypoxia-inducible factor 1. *Semin. Cancer Biol.* 2009, *19*. 12-16, DOI: 10.1016/j.semcancer.2008.11.009.
17. R. Venkatasubramanian, M. A. Henson, N. S. Forbes, Incorporating energy metabolism into a growth model of multicellular tumor spheroids. *Journal of theoretical biology* 2006, *242*. 440-53, DOI: 10.1016/j.jtbi.2006.03.011.
18. B. J. Kim, N. S. Forbes, Flux analysis shows that hypoxia-inducible-factor-1-alpha minimally affects intracellular metabolism in tumor spheroids. *Biotechnology and Bioengineering* 2007, *96*. 1167-1182.
19. (a) H. Acker, J. Carlsson, W. Mueller-Klieser, R. M. Sutherland, Comparative pO2 measurements in cell spheroids cultured with different techniques. *Br J Cancer* 1987, *56*. 325-7; (b) R. M. Sutherland, B. Sordat, J. Bamat, H. Gabbert, B. Bourrat, W. Mueller-Klieser, Oxygenation and differentiation in multicellular spheroids of human colon carcinoma. *Cancer Res* 1986, *46*. 5320-9.
20. W. Mueller-Klieser, Multicellular spheroids. A review on cellular aggregates in cancer research. *J Cancer Res Clin Oncol* 1987, *113*. 101-22.
21. J. Carlsson, H. Acker, Influence of the oxygen pressure in the culture medium on the oxygenation of different types of multicellular spheroids. *International journal of radiation oncology, biology, physics* 1985, *11*. 535-46.
22. B. J. Toley, J. Park, B. J. Kim, R. Venkatasubramanian, M. M. Maharbiz, N. S. Forbes, Micrometer-scale oxygen delivery rearranges cells and prevents necrosis in tumor tissue in vitro. *Biotechnol Prog* 2011, *DOI: 10.1002/btpr.1510*. DOI: 10.1002/btpr.1510.
23. D. B. Papkovsky, R. I. Dmitriev, Biological detection by optical oxygen sensing. *Chem Soc Rev* 2013, *42*. 8700-32, DOI: 10.1039/c3cs60131e.

24. (a) D. Lambrechts, M. Roeffaers, G. Kerckhofs, S. J. Roberts, J. Hofkens, T. Van de Putte, H. Van Oostervvyck, J. Schrooten, Fluorescent oxygen sensitive microbead incorporation for measuring oxygen tension in cell aggregates. *Biomaterials* 2013, *34*. 922-929, DOI: 10.1016/j.biomaterials.2012.10.019; (b) R. I. Dmitriev, A. V. Zhdanov, Y. M. Nolan, D. B. Papkovsky, Imaging of neurosphere oxygenation with phosphorescent probes. *Biomaterials* 2013, *34*. 9307-17, DOI: 10.1016/j.biomaterials.2013.08.065.
25. J. J. Casciari, S. V. Sotirchos, R. M. Sutherland, Mathematical modelling of microenvironment and growth in EMT6/Ro multicellular tumour spheroids. *Cell proliferation* 1992, *25*. 1-22.
26. R. A. Gatenby, R. J. Gillies, Why do cancers have high aerobic glycolysis? *Nature Reviews Cancer* 2004, *4*. 891-899, DOI: 10.1038/nrc1478.
27. R. J. DeBerardinis, J. J. Lum, G. Hatzivassiliou, C. B. Thompson, The biology of cancer: Metabolic reprogramming fuels cell growth and proliferation. *Cell Metab.* 2008, *7*. 11-20, DOI: 10.1016/j.cmet.2007.10.002.
28. (a) S. Walenta, T. Schroeder, W. Mueller-Klieser, Metabolic mapping with bioluminescence: basic and clinical relevance. *Biomol Eng* 2002, *18*. 249-62; (b) B. J. Kim, N. S. Forbes, Flux analysis shows that hypoxia-inducible-factor-1-alpha minimally affects intracellular metabolism in tumor spheroids. *Biotechnol Bioeng* 2006.
29. N. S. Forbes, A. L. Meadows, D. S. Clark, H. W. Blanch, Estradiol stimulates the biosynthetic pathways of breast cancer cells: detection by metabolic flux analysis. *Metabolic engineering* 2006, *8*. 639-52, DOI: 10.1016/j.ymben.2006.06.005.
30. R. C. Poole, A. P. Halestrap, Transport of lactate and other monocarboxylates across mammalian plasma-membranes. *Am. J. Physiol.* 1993, *264*. C761-C782.
31. R. S. Brown, R. L. Wahl, Overexpression of GLUT-1 glucose-transporter in human breast-cancer - an immunohistochemical study. *Cancer* 1993, *72*. 2979-2985, DOI: 10.1002/1097-0142(19931115)72:10<2979::aid-cncr2820721020>3.0.co;2-x.
32. C. K. Garcia, J. L. Goldstein, R. K. Pathak, R. G. W. Anderson, M. S. Brown, Molecular characterization of a membrane transporter for lactate, pyruvate, and other monocarboxylates - implications for the cori cycle. *Cell* 1994, *76*. 865-873, DOI: 10.1016/0092-8674(94)90361-1.
33. R. Le Floch, J. Chiche, I. Marchiq, T. Naiken, K. Ilk, C. M. Murray, S. E. Critchlow, D. Roux, M. P. Simon, J. Pouyssegur, CD147 subunit of lactate/H+ symporters MCT1 and hypoxia-inducible MCT4 is critical for energetics and growth of glycolytic tumors. *Proceedings of the National Academy of Sciences of the United States of America* 2011, *108*. 16663-16668, DOI: 10.1073/pnas.1106123108.
34. P. Sonveaux, F. Vegran, T. Schroeder, M. C. Wergin, J. Verrax, Z. N. Rabbani, C. J. De Saedeleer, K. M. Kennedy, C. Diepart, B. F. Jordan, M. J. Kelley, B. Gallez, M. L. Wahl, O. Feron, M. W. Dewhirst, Targeting lactate-fueled respiration selectively kills hypoxic tumor cells in mice. *Journal of Clinical Investigation* 2008, *118*. 3930-3942, DOI: 10.1172/jci36843.
35. P. R. Young, S. M. Spevacek, Substratum acidification and proteinase activation by murine B16F10 melanoma cultures. *Biochim Biophys Acta* 1993, *1182*. 69-74.
36. E. K. Rofstad, K. Eide, R. Skoyum, M. E. Hystad, H. Lyng, Apoptosis, energy metabolism, and fraction of radiobiologically hypoxic cells: a study of human melanoma multicellular spheroids. *Int J Radiat Biol* 1996, *70*. 241-9.
37. (a) R. J. DeBerardinis, A. Mancuso, E. Daikhin, I. Nissim, M. Yudkoff, S. Wehrli, C. B. Thompson, Beyond aerobic glycolysis: Transformed cells can engage in glutamine metabolism that exceeds the requirement for protein and nucleotide synthesis. *Proceedings of the National*

Academy of Sciences of the United States of America 2007, *104*. 19345-19350, DOI: 10.1073/pnas.0709747104; (b) S. M. Jeong, C. Y. Xiao, L. W. S. Finley, T. Lahusen, A. L. Souza, K. Pierce, Y. H. Li, X. X. Wang, G. Laurent, N. J. German, X. L. Xu, C. L. Li, R. H. Wang, J. Lee, A. Csibi, R. Cerione, J. Blenis, C. B. Clish, A. Kimmelman, C. X. Deng, M. C. Haigis, SIRT4 Has Tumor-Suppressive Activity and Regulates the Cellular Metabolic Response to DNA Damage by Inhibiting Mitochondrial Glutamine Metabolism. *Cancer Cell* 2013, *23*. 450-463, DOI: 10.1016/j.ccr.2013.02.024; (c) C. M. Metallo, P. A. Gameiro, E. L. Bell, K. R. Mattaini, J. J. Yang, K. Hiller, C. M. Jewell, Z. R. Johnson, D. J. Irvine, L. Guarente, J. K. Kelleher, M. G. Vander Heiden, O. Iliopoulos, G. Stephanopoulos, Reductive glutamine metabolism by IDH1 mediates lipogenesis under hypoxia. *Nature* 2012, *481*. 380-U166, DOI: 10.1038/nature10602.

38. J. W. Wojtkowiak, J. M. Rothberg, V. Kumar, K. J. Schramm, E. Haller, J. B. Proemsey, M. C. Lloyd, B. F. Sloane, R. J. Gillies, Chronic Autophagy Is a Cellular Adaptation to Tumor Acidic pH Microenvironments. *Cancer Research* 2012, *72*. 3938-3947, DOI: 10.1158/0008-5472.can-11-3881.

39. V. Estrella, T. A. Chen, M. Lloyd, J. Wojtkowiak, H. H. Cornnell, A. Ibrahim-Hashim, K. Bailey, Y. Balagurunathan, J. M. Rothberg, B. F. Sloane, J. Johnson, R. A. Gatenby, R. J. Gillies, Acidity Generated by the Tumor Microenvironment Drives Local Invasion. *Cancer Research* 2013, *73*. 1524-1535, DOI: 10.1158/0008-5472.can-12-2796.

40. (a) N. S. Forbes, A. L. Meadows, D. S. Clark, H. W. Blanch, Estradiol stimulates the biosynthetic pathways of breast cancer cells: detection by metabolic flux analysis. *Metab Eng* 2006, *8*. 639-52; (b) M. G. Hunnewell, N. S. Forbes, Active and inactive metabolic pathways in tumor spheroids: determination by GC-MS. *Biotechnol Prog* 2010, *26*. 789-96, DOI: 10.1002/btpr.360; (c) D. R. Wise, R. J. DeBerardinis, A. Mancuso, N. Sayed, X. Y. Zhang, H. K. Pfeiffer, I. Nissim, E. Daikhin, M. Yudkoff, S. B. McMahon, C. B. Thompson, Myc regulates a transcriptional program that stimulates mitochondrial glutaminolysis and leads to glutamine addiction. *Proceedings of the National Academy of Sciences of the United States of America* 2008, *105*. 18782-18787, DOI: 10.1073/pnas.0810199105; (d) A. Csibi, S. M. Fendt, C. G. Li, G. Poulogiannis, A. Y. Choo, D. J. Chapski, S. M. Jeong, J. M. Dempsey, A. Parkhitko, T. Morrison, E. P. Henske, M. C. Haigis, L. C. Cantley, G. Stephanopoulos, J. Yu, J. Blenis, The mTORC1 Pathway Stimulates Glutamine Metabolism and Cell Proliferation by Repressing SIRT4. *Cell* 2013, *153*. 840-854, DOI: 10.1016/j.cell.2013.04.023; (e) R. J. DeBerardinis, N. Sayed, D. Ditsworth, C. B. Thompson, Brick by brick: metabolism and tumor cell growth. *Curr. Opin. Genet. Dev.* 2008, *18*. 54-61, DOI: 10.1016/j.gde.2008.02.003.

41. P. A. Netti, D. A. Berk, M. A. Swartz, A. J. Grodzinsky, R. K. Jain, Role of extracellular matrix assembly in interstitial transport in solid tumors. *Cancer Res* 2000, *60*. 2497-503.

42. J. P. Freyer, R. M. Sutherland, Selective dissociation and characterization of cells from different regions of multicell tumor spheroids. *Cancer Res* 1980, *40*. 3956-65.

43. R. J. Early, J. R. Thompson, G. W. Sedgwick, J. M. Kelly, R. J. Christopherson, Capillary gas chromatographic analysis of amino acids in blood and protein hydrolysates as tert.-butyldimethylsilyl derivatives. *J Chromatogr* 1987, *416*. 15-23.

44. M. Hockel, P. Vaupel, Tumor hypoxia: definitions and current clinical, biologic, and molecular aspects. *J Natl Cancer Inst* 2001, *93*. 266-76.

45. R. Venkatasubramanian, M. A. Henson, N. S. Forbes, Incorporating energy metabolism into a growth model of multicellular tumor spheroids. *J Theor Biol* 2006, *242*. 440-53.

46. G. Helmlinger, A. Sckell, M. Dellian, N. S. Forbes, R. K. Jain, Acid production in glycolysis-impaired tumors provides new insights into tumor metabolism. *Clinical cancer research : an official journal of the American Association for Cancer Research* 2002, *8*. 1284-91.
47. R. Venkatasubramanian, M. a. Henson, N. S. Forbes, Incorporating energy metabolism into a growth model of multicellular tumor spheroids. *Journal of theoretical biology* 2006, *242*. 440-53, DOI: 10.1016/j.jtbi.2006.03.011.
48. N. S. Forbes, A. L. Meadows, D. S. Clark, H. W. Blanch, Estradiol stimulates the biosynthetic pathways of breast cancer cells: detection by metabolic flux analysis. *Metabolic Engineering* 2006, *DOI:10.1016/j.ymben.2006.06.005*.
49. (a) G. Helmlinger, F. Yuan, M. Dellian, R. K. Jain, Interstitial pH and pO2 gradients in solid tumors in vivo: high-resolution measurements reveal a lack of correlation. *Nat Med* 1997, *3*. 177-82; (b) M. Yamagata, K. Hasuda, T. Stamato, I. F. Tannock, The contribution of lactic acid to acidification of tumours: studies of variant cells lacking lactate dehydrogenase. *Br J Cancer* 1998, *77*. 1726-31; (c) K. Newell, A. Franchi, J. Pouyssegur, I. Tannock, Studies with glycolysis-deficient cells suggest that production of lactic acid is not the only cause of tumor acidity. *Proc Natl Acad Sci U S A* 1993, *90*. 1127-31.

Figures

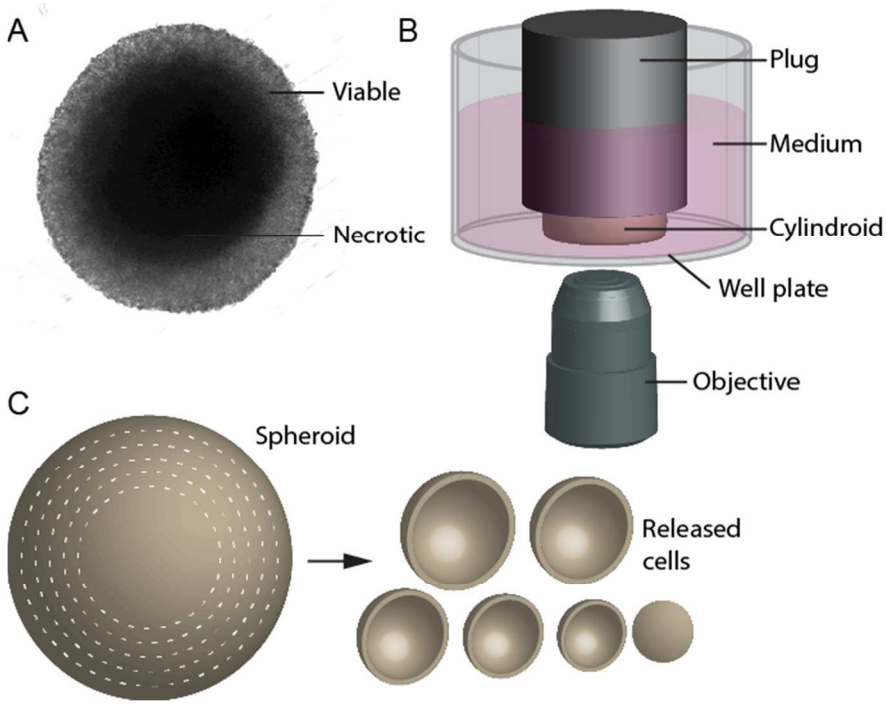

Figure 1. In vitro tumor-mimicking techniques: cylindroids and spheroid dissociation
A) Image of a multicellular tumor spheroid, with a transparent viable periphery and an opaque necrotic core. B) Tumor cylindroids are formed by constraining spheroids between the bottom of a well plate and a plug attached to the well-plate lid. Plugs are spaced 150 μm above the bottom of the plate. The wells are filled medium and interior regions of cylindroids can be observed from the underside by microscopy. C) The metabolic content of cells as a function of radius is determined by successive rounds of dissociation that isolated cells from concentric shells.

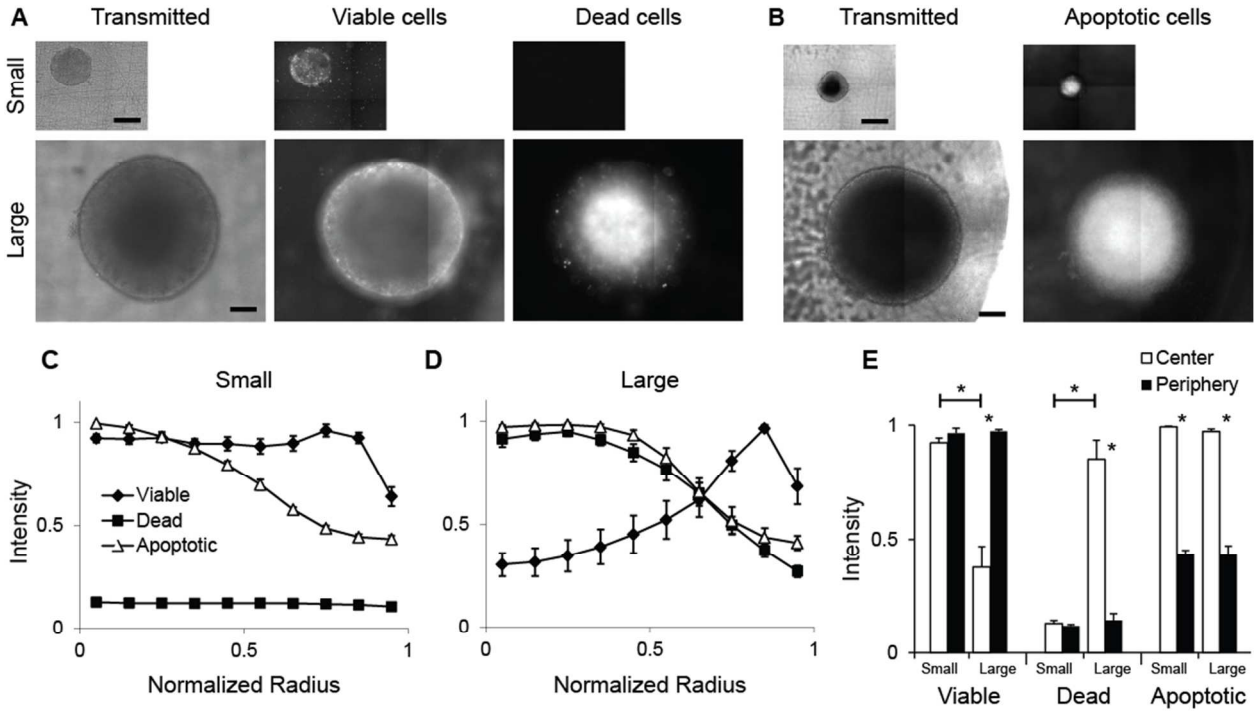

Figure 2. Distribution of cell viability and apoptosis in small and large cylindroids. A) Transmitted and fluorescence images of a small and large cylindroid. Fluorescence images show location of viable and dead cells using the Live/Dead cell viability assay. Scale bars are 200 μm. B) Transmitted and fluoresce images of a small and large cylindroids stained to identify activated caspase-3, an indicator of apoptosis. C,D) Radial profiles of viable cells, necrotic cells, and cells with activated caspase-3 in populations of small (*C*; diameter<500 μm; *n*=5 for Live/Dead; *n*=6 for apoptosis) and large (*D*; diameter>500 μm*; n*=5 for live/dead; *n*=3 for apoptosis) cylindroids. Some errors are small and the bars are obscured by data markers. E) Extent of viability, necrosis and apoptosis in the interior and peripheral 10% of the cylindroid populations. Cell viability was greater in the center of small compared to large cylindroids (*, P<0.001); cell death was greater in the center of large cylindroids (*, P<0.001); and apoptosis was greater in the center compared to the periphery for both small and large cylindroids (*, P<0.001). In large cylindroids, viability was greater in the periphery (*, P<0.001), and death was greater in the center (*, P<0.001).

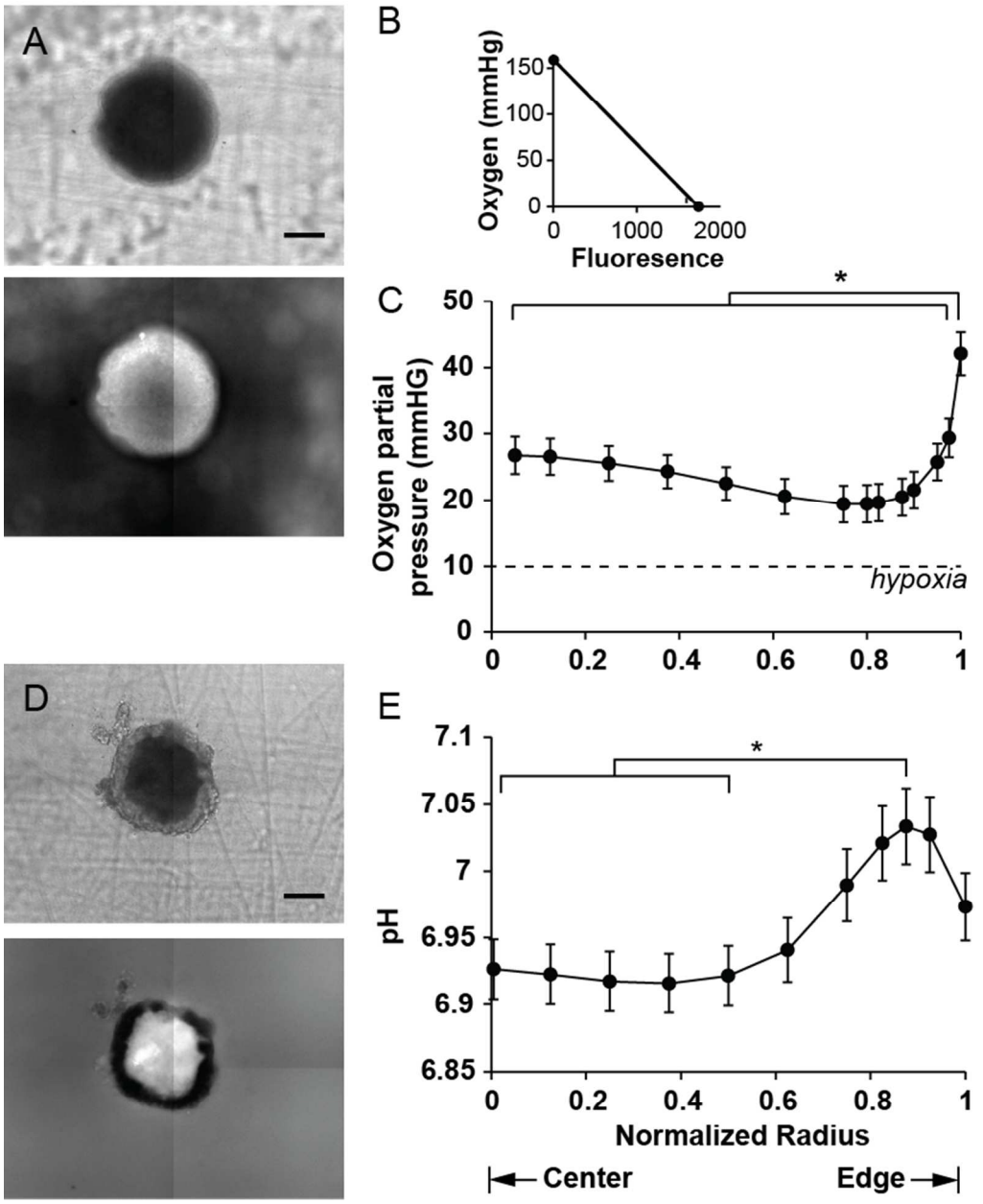

Figure 3. Oxygen concentration and extracellular pH profiles in tumor cylindroids. A) Transmitted and fluorescence images of a cylindroid stained with ruthenium-tris(4,7-diphenyl-1,10-phenanthroline) dichloride. Brightness in the fluorescence image is inverse to oxygen concentration. Bright regions have lower oxygen concentrations and dark regions have more oxygen. B) Two-point calibration of Ru-dpp in DMEM in ambient air (159 mmHg O_2) and pure nitrogen (0 mmHg O_2). C) Oxygen partial-pressure (pO_2) radial profile of tumors cylindroids (n=14). Error bars represent standard error of the mean. The oxygen concentration at normalized radii less than 0.975 was lower than at the edge (*, P<0.01). D) Transmitted and fluorescence images of a cylindroid stained with BCECF. E) Radial pH profile in tumors cylindroids (n=54). The pH at normalized radii between 0 and 0.5 was lower than at 0.875 (*, P<0.005). Error bars represent standard error of the mean.

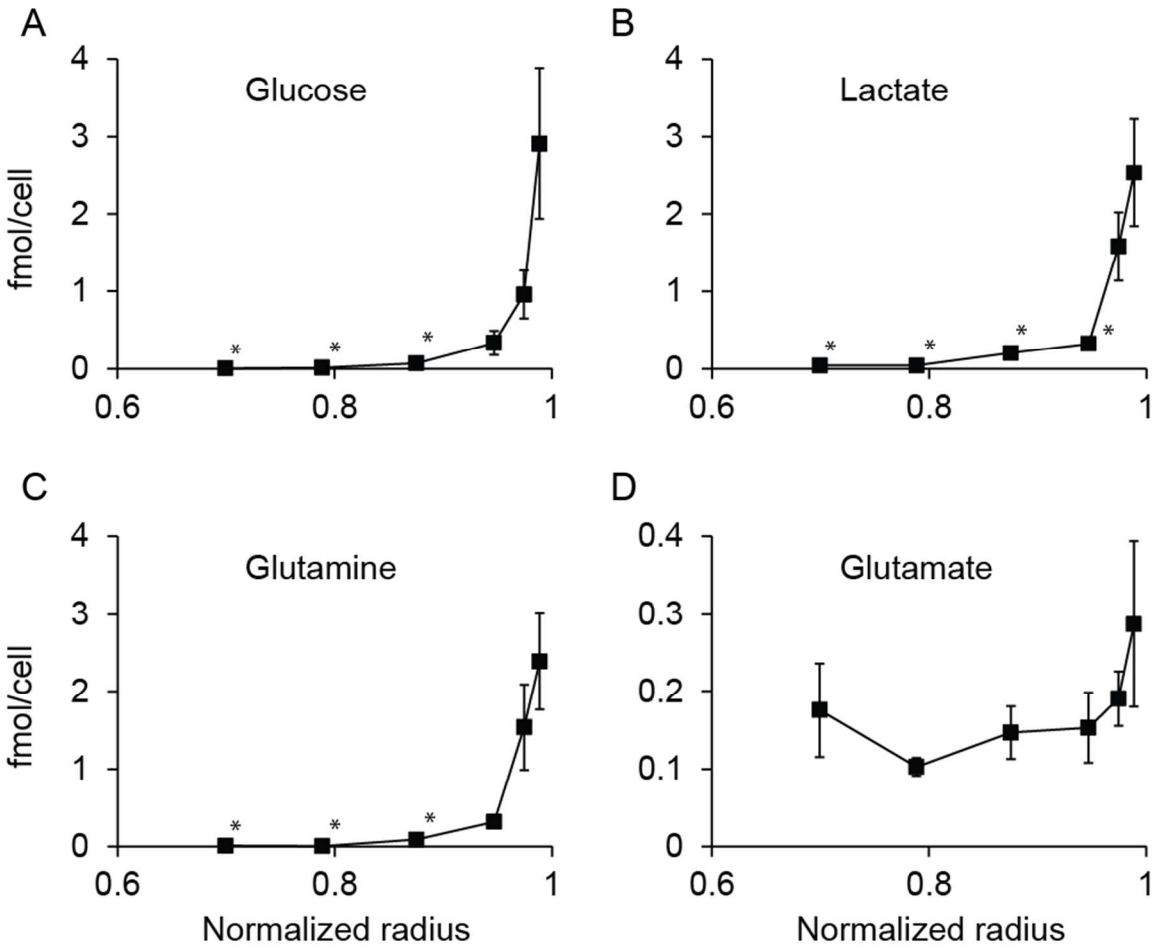

Figure 4. Concentration profiles of four intracellular metabolites in spheroids. Profiles of (*A*) glucose, (*B*) lactate, (*C*) glutamine and (*D*) glutamate as functions of normalized radius (n=3). The average spheroid radius was 287μm. Each point represents a single layer of cells removed from the outer edge of a group of spheroids. The concentrations of glucose and glutamine (*A*, *C*) in the inner three layers was lower than the outer edge (*, $P<0.05$). The concentration of lactate (*B*) was lower in the inner four layers than the edge (*, $P<0.05$). The concentration of glutamate (*D*) did not decrease with radius. Error bars represent standard error of mean.

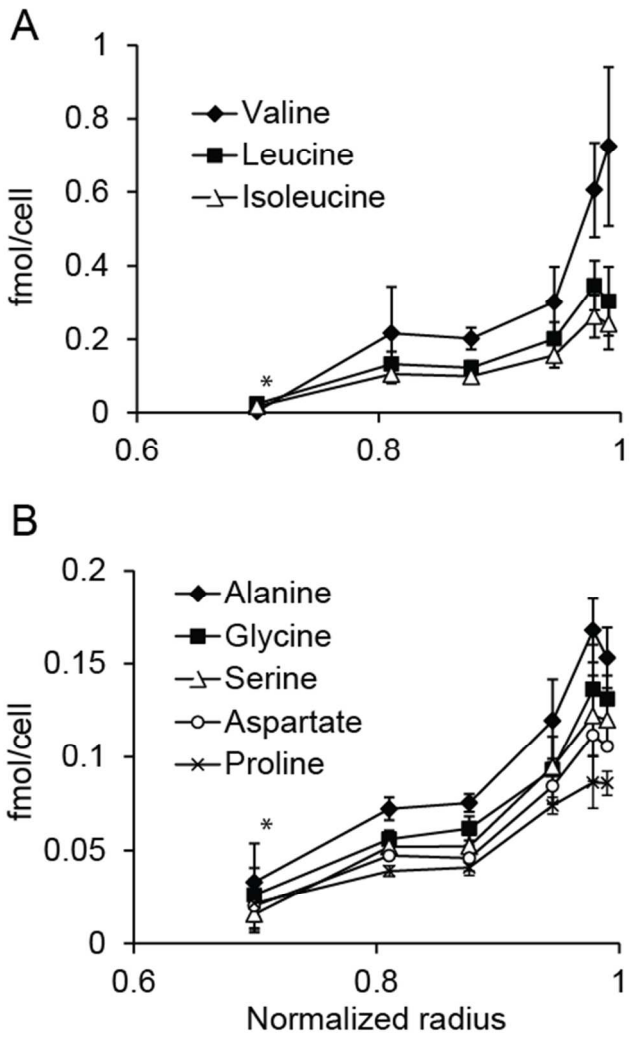

Figure 5. Concentration profiles of intracellular amino acids in spheroids. A) Radial concentration profiles of three essential amino acids: valine, leucine, and isoleucine (*n*=3). Concentrations of all three were lower at a normalized radius of 0.70 than at the outer edge (*, P<0.05). B) Radial concentration profiles of five non-essential amino acids: alanine, glycine, proline, serine, and aspartate (*n*=3). Concentrations of all five were lower at a normalized radius of 0.70 than at the outer edge (*, P<0.05).

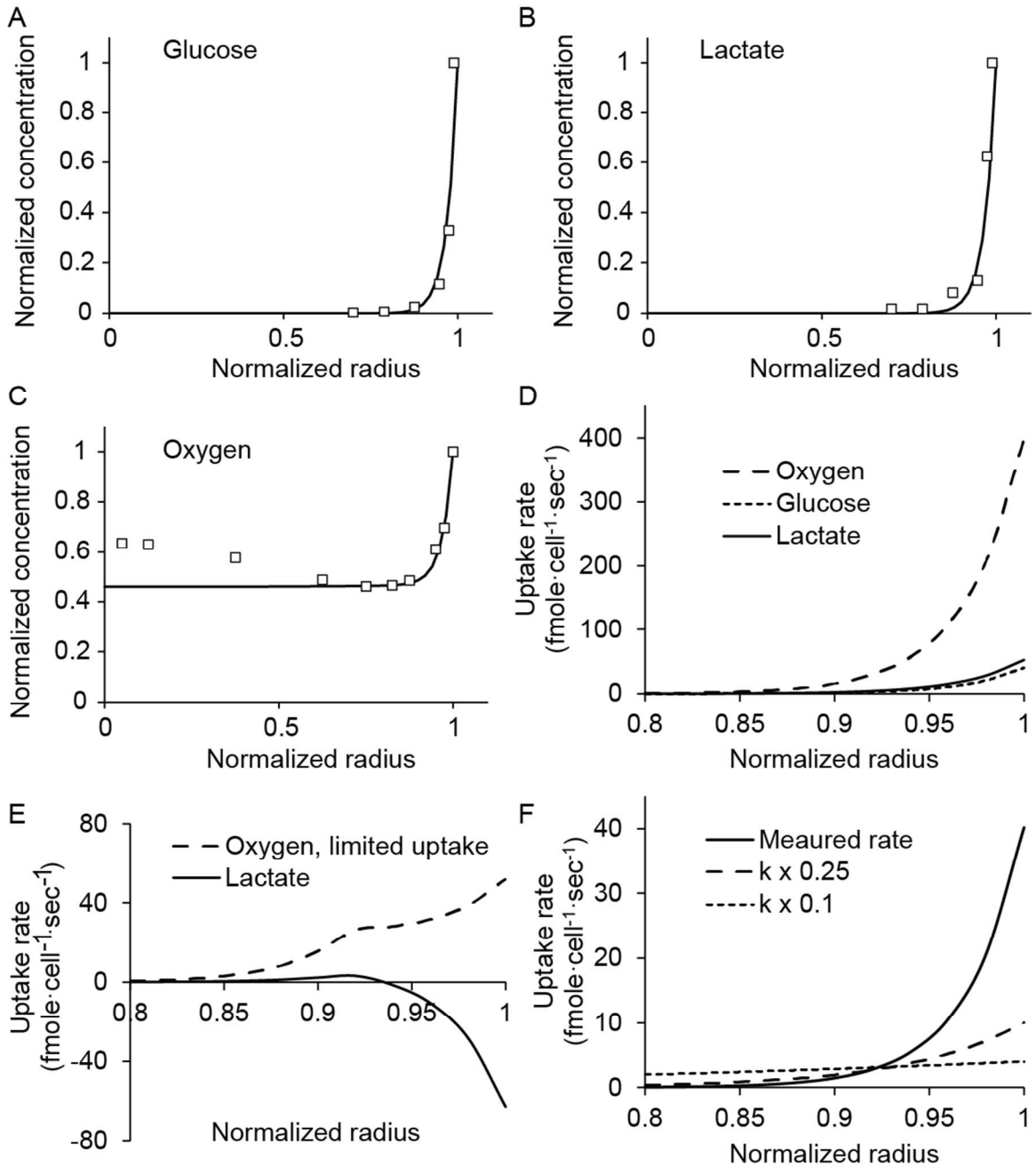

Figure 6. Computational analysis of metabolism and diffusion. A-C) Measured values and computational predictions of concentrations for *(A)* glucose, *(B)* lactate, and *(C)* oxygen. For both the measurements and the model, glucose and lactate were completely consumed at the edge and oxygen was present in the center. D) Uptake rates of oxygen, glucose, and lactate as a function of radius. Oxygen uptake was greater than glucose and lactate because of the stoichiometry of intracellular metabolism. E) Effect of hypothetically limiting cellular uptake of oxygen. Oxygen uptake would be reduced at the outer edge, and lactate would have been produced, rather than consumed. F) Effect of reducing the glucose rate constant (k) on uptake as

a function of radius. At the edge, consumption would be reduced, but in the center it would be increased.